

‘UNIFIED’ LAGUERRE-POWER MESHES FOR COUPLED EARTH SYSTEM MODELLING

Darren Engwirda^{1,*} Chang Liao²

¹*Theoretical Division, Los Alamos National Laboratory,
Los Alamos, NM, USA, **

²*Atmospheric Sciences and Global Change, Pacific Northwest National Laboratory,
Richland, WA, USA*

ABSTRACT

The representation of physical processes in earth system models is often constrained and simplified by details of the underlying numerical model. Ocean, atmosphere, ice, land and river dynamics are typically discretised over incompatible computational grids, and are coupled together via ‘lossy’ interpolation schemes. In this work, we describe an alternative ‘unified’ approach, in which components are represented on a common multi-scale unstructured mesh, and employ compatible numerical formulations and ‘interpolation-free’ coupling across embedded boundaries. This unified strategy is built on an unstructured primal-dual meshing workflow, in which a global surface mesh conforming to various coastline, river network and land process boundaries is formed as a ‘restricted’ Laguerre-Power tessellation. This mesh layout enables coupled physics to be discretised over the set of staggered edge-, triangle- and cell-based control-volumes, leading to a conforming representation. Key to this process is the use of restricted triangulations to approximate complex boundaries and constraints in a multi-scale manner, enabling a transition from high-resolution regional representations to coarser global scales. Initial work on the ‘unified’ representation is reported here, focusing on development of the restricted triangulation kernels, and subsequent staggered Laguerre-Power mesh optimisation techniques.

Keywords: Restricted filtration, Laguerre-Power tessellation, Earth system modelling

1. INTRODUCTION

The development of variable-resolution earth system models based on unstructured meshes and numerical methods is an emerging area of study, typified by several large-scale efforts including the US Department of Energy’s E3SM framework [1], and the FESOM + ECHARM system [2] developed jointly by Germany’s Alfred Wegner and Max Planck Institutes. Central to the construction of such models are choices concerning the underlying computational mesh and discretisation framework. Conventionally, earth system models have taken a ‘decentralised’ approach — nesting discretisations for various physical processes (ocean,

atmosphere, river, land, ice) throughout the global domain via a set of partially-overlapping structured grids. While such an approach enables the development of models for each physical process individually, significant issues arise when seeking to simulate coupled dynamics — requiring the use of various interpolation strategies to compute fluxes between components (e.g. river-to-ocean, land-to-river, etc). Maintaining conservation of mass, energy, heat, etc, throughout the coupled system in such configurations represents a source of ongoing difficulty in coupled climate modelling.

In this work, an alternative strategy is pursued, in which numerous earth system components are discretised using a common ‘unified’ unstructured global

*Corresponding author: dengwirda@lanl.gov

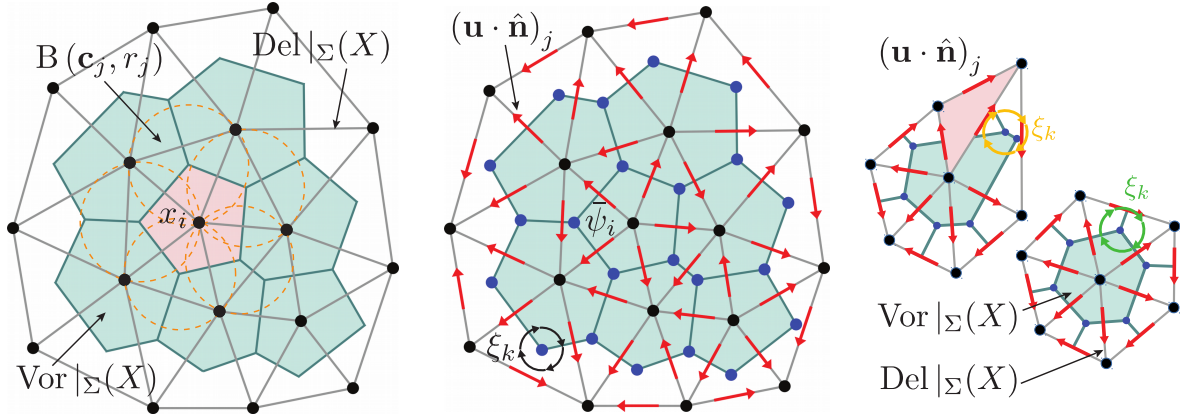


Figure 1: The staggered ‘TRSK’ discretisation used in the MPAS framework. Mass DoF are positioned within polygonal cells, normal velocities are staggered along triangle edges, and fluid circulation is computed over dual triangles. The rightmost panel shows difficulties associated with obtuse triangles — ‘well-centred’ staggering is required for numerical consistency.

mesh. In addition to support for variable-resolution, such an approach facilitates the use of consistent numerical discretisations — enabling ‘interpolation-free’ coupling at embedded boundaries, and eliminating the associated issues regarding conservation. In the following, we outline the development of our underlying ‘unified’ mesh generation strategy, based on the construction of a class of orthogonal primal-dual meshes (Laguerre-Power tessellations [14, 15]) to define a set of staggered edge-, triangle- and polygon-centred control-volumes appropriate for finite-volume type numerical schemes. Key to our meshing strategy is the use of ‘restricted’ tessellation techniques [28, 34, 29] to enable the approximation of embedded boundaries (coastlines, river networks, land-process regions, etc) across varying spatial resolution. In addition to mesh construction, we detail our weighted mesh optimisation scheme, designed to generate high-quality centroidal Laguerre-Power tessellations with the aim of minimising numerical errors associated with second-order accurate finite-volume type approximations.

2. GRIDS, STAGGERING AND DISCRETISATION

The Model for Prediction Across Scales (MPAS) [16, 18] is a staggered ‘mimetic’ discretisation scheme, presently used to represent both ocean [17] and atmospheric processes [19] in global climate and weather forecast models. The scheme distributes various mass-, velocity- and circulation-based degrees-of-freedom across a set of staggered orthogonal control volumes (see Figure 1), requiring the generation of orthogonal primal-dual meshes. We use the so-called Laguerre-Power primal-dual [14, 15], which is an ex-

tension of the well-known Delaunay-Voronoi tessellation. Additional details regarding Laguerre triangulations and Power diagrams will be included in subsequent sections.

In addition to ocean and atmospheric dynamics, we adopt a new MPAS-like discretisation for river and land processes here — integrating land-based physics within polygonal cells, and routing river flows along triangle edges. Such a staggered discretisation enables various direct coupling between models: river-ocean fluxes can be exchanged across cell boundaries (along triangle edges), land-river fluxes can be exchanged between the river segments embedded with each cell, and the ocean can dynamically flood across land cells. We do not seek to provide a detailed description of the earth system model physics or discretisation here, but rather focus on the enabling meshing strategy. Interested readers are referred to the Model for Prediction Across Scales (MPAS) [17], the MOdel for Scale Adaptive River Transport (MOSART) [1] and the E3SM Land Model (ELM) [1] for additional detail.

From a meshing perspective, the MPAS-type numerical discretisation imposes several key constraints: (a) the primal-dual staggering must be orthogonal, such that paired triangle and polygon edges are perpendicular, (b) the primal and dual cells must be approximately centroidal, such that triangle vertices lie near polygon centroids and visa-versa and (c) the triangulation must be ‘well-centred’, such that all triangles contain their paired polygon vertex. The first constraint emanates from the decomposition of fluxes across cell boundaries based only on normal velocity components, while the second and third constraints relate to the accuracy and consistency of the numerical scheme. The

use of centroidal tessellations enables the staggered discretisation to achieve approximately second-order spatial accuracy, and well-centredness guarantees that transport and circulation operators are well posed by ensuring that paired triangle and polygon edges have non-null intersections. See [13] for an extended discussion of the accuracy and characteristics of MPAS-type discretisations.

3. LAGUERRE TRIANGULATIONS AND POWER DIAGRAMS

To satisfy the constraints of the MPAS-type discretisation described in the previous section, we adopt a primal-dual mesh based on a Laguerre-Power pair, also sometimes referred to as a *Regular triangulation* or a *Dirichlet cell complex* [14]. Such meshes are a generalisation of the well-known Delaunay-Voronoi tessellation, and consist of a ‘weighted’ Laguerre triangulation and its orthogonal Power diagram [14, 15]. Extending the standard Voronoi diagram, Power cells are defined in terms of the weighted Power distance

Definition 1 (Weighted points & power distance). A *weighted* point set is defined as a pair $(\mathbf{X}, W) = \{(\mathbf{x}_1, w_1), (\mathbf{x}_2, w_2), \dots, (\mathbf{x}_n, w_n)\}$, where $\{\mathbf{x}_i\} \subset \mathbb{R}^d$ are a set of points embedded in d -dimensional Euclidean space and $\{w_i\} \subset \mathbb{R}$ are an associated set of scalar weights. The *power distance* [14], herein denoted $\pi_i(\mathbf{x})$, between an unweighted point $\mathbf{x} \in \mathbb{R}^d$ and a weighted point (\mathbf{x}_i, w_i) is defined as $\pi_i(\mathbf{x}) = \|\mathbf{x} - \mathbf{x}_i\|^2 - w_i$, where $\|\cdot\|$ is the standard Euclidean distance operator.

Definition 2 (Laguerre-Power tessellation). Given a weighted point set (\mathbf{X}, W) , the *Power complex* [14] $\text{Pow}(\mathbf{X}, W)$ is the union of polygonal cells $\{P_i\}$, where each $P_i = \{\mathbf{x} \in \mathbb{R}^d \mid \pi_i(\mathbf{x}) < \pi_j(\mathbf{x}), \forall j \neq i\}$. The associated primal complex $\text{Tri}(\mathbf{X}, W)$ is a simplicial triangulation of the weighted points (\mathbf{X}, W) , consisting of the union of simplexes $\{\tau_k\}$, where each τ_k contains the vertices $\{\mathbf{x}_1, \mathbf{x}_2, \dots, \mathbf{x}_k\} \in \mathbf{X}$ iff $\bigcap_{j=1}^{j=k} D_j \neq \emptyset$ [6]. The primal complex is known as the *Laguerre triangulation* of the weighted points (\mathbf{X}, W) .

The Power complex is a Voronoi-like subdivision of space, where each cell $P_i \in \text{Pow}(\mathbf{X}, W)$ defines a convex region $\mathbf{x} \subseteq \mathbb{R}^d$ for which the weighted point (\mathbf{x}_i, w_i) is *closer*, in a weighted sense, than all other points in (\mathbf{X}, W) . The theory of Power complexes and Laguerre tessellations has been developed previously, and the reader is referred to, for example, Aurenhammer [14] and Edelsbrunner [15] for additional detail.

Our interest in Laguerre-Power meshes is due to the work of Mullen et al [6, 5, 7], who introduced the notion of Hodge Optimised Triangulations (HOT) to

improve the accuracy of discretisations based on Discrete Exterior Calculus (DEC). Previous work [3] has shown equivalence between the mimetic formulation used by MPAS and DEC-based schemes, encouraging the use of related mesh optimisation principles to develop high-quality grids for our MPAS-based earth system model. In particular, Mullen et al have shown that through careful selection of the vertex weights in a Laguerre-Power tessellation, the ‘quality’ of staggering between triangles and dual cells can be improved, leading to highly centroidal meshes appropriate for the staggered numerical discretisations described here (see Figure 2) Previous work [13] has also shown that the use of such weighted optimisation techniques can lead to well-centred tessellations — a difficult outcome for general unstructured meshes [20, 21]. In summary, we pursue the use of weighted Laguerre-Power tessellations in preference to the standard Delaunay-Voronoi paradigm in order to optimise the performance of the mimetic MPAS-type discretisation scheme used in our modelling framework, which benefits from staggered orthogonal meshes that are both centroidal and well-centred. Our weighted mesh optimisation scheme will be described in subsequent sections.

4. BOUNDARIES AND RESTRICTED TRIANGULATIONS

The generation of meshes conforming to a complex network of inter-component boundaries is a key aspect of our unified workflow. Boundaries consist of ‘polyarc’ networks — arc-segments inscribed on the ellipsoidal mean-earth surface, representing various coastlines, river networks, watersheds and other land and ocean-process boundaries. While the generation of meshes constrained to polylines (or polyarcs on the spheroid) is not new, such ‘direct’ approaches often do not lead to useful results for geoscientific problems, where data-sets often contain a multitude of features undesirable for mesh generation (being sampled at inappropriate resolution, containing sharp corners and/or narrow passages, and self-intersecting segments). The application of conventional meshing tools (e.g. Triangle [9]) typically results in low-quality grids — containing large numbers of unnecessarily small cells in an effort to capture undesirable features in the input geometry. The presence of these artefacts can impose severe restrictions on model time-step (our framework is based on explicit time integration strategies) and an optimal mesh should instead ‘filter-out’ these features and sample the domain at length scales of interest. While pre-processing techniques can be applied to smooth and simplify input geometry, it is often difficult to obtain results that lead to optimal meshes, especially when complex non-uniform mesh-spacing constraints are imposed, as is typical in earth system model configurations.

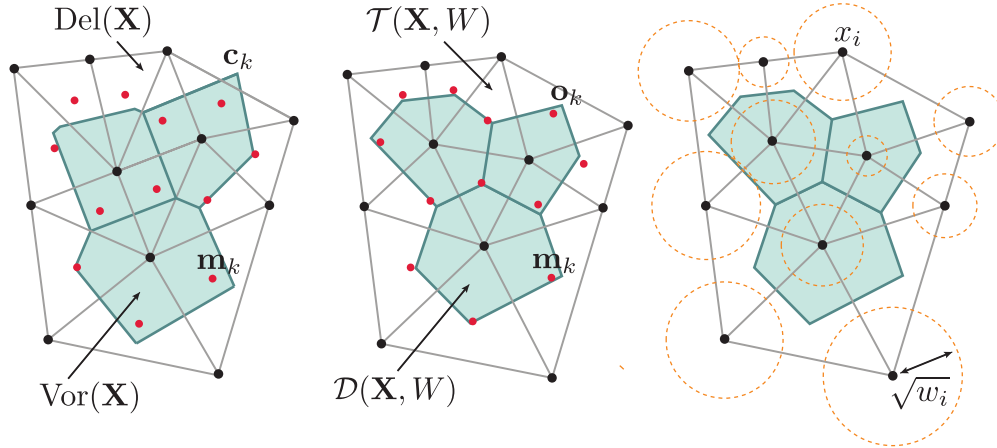


Figure 2: Comparison of Delaunay-Voronoi and Laguerre-Power tessellations, showing the additional improvement in cell shape and centroidal staggering possible through optimisation of the Laguerre weights. Triangle centroids are drawn as red points. The distribution of vertex weights is shown in the rightmost panel, as circles of radius $\sqrt{w_i}$.

Instead, we pursue the use of ‘restricted’ triangulation techniques [28, 29] to generate meshes that conform ‘approximately’ to a given boundary definition, based on the length scales defined by the user. Such methods do not seek to triangulate the full input geometry exactly, but instead progressively refine an initially coarse tessellation until a satisfactory approximation is obtained. This triangulation is then further refined to ensure a suite of mesh-spacing and cell-quality constraints are satisfied, leading to high-quality tessellations that effectively ‘filter-out’ small, undesirable features in the geometry definition. See Figure 3 for detail, in which geometrical features (bays, inlets, passages, etc) sufficiently smaller than the local user-defined mesh-spacing lengths are eliminated from the resulting triangulation.

Restricted triangulation techniques have been investigated by a number of authors in recent years, commonly in the domain of surface mesh generation [33, 30, 34, 10]. A restricted triangulation is a hierarchy of sub-complexes — designed to provide multi-scale approximations to embedded geometrical features. The hierarchy consists of a bounding convex triangulation $\text{Tri}(\mathbf{X}, W)$, in this case a surface mesh of the ellipsoidal mean-earth domain, as well as a series of embedded sub-triangulations that approximate geometrical features. In this case, a single sub-triangulation $\text{Tri}_\Gamma(\mathbf{X}, W)$ is needed, to represent the set of edges $e \in \text{Tri}(\mathbf{X}, W)$ that approximate the various polyarc boundaries described by Γ (coastlines, river networks, etc). An edge e is part of the restricted sub-complex $\text{Tri}_\Gamma(\mathbf{X}, W)$ if its paired dual face $p_f \in \text{Pow}(\mathbf{X}, W)$ intersects a segment in the boundary set Γ . An overview of restricted tessellation

techniques is provided in, for example [31, 30, 34].

Each edge in the restricted sub-complex $\text{Tri}_\Gamma(\mathbf{X}, W)$ is also associated with a circumscribing ball — a so-called *Surface Laguerre Ball* $\text{SLB}(e_i)$. These balls are the weighted circumscribing spheres centred upon intersections of the associated Power dual and the input geometry. In the case of multiple intersections, the corresponding ball of maximum radius is selected. See Figure 5, 6 for detail. The geometry of such balls provides a measure of fidelity of approximation — an estimate for how well the edges $e \in \text{Tri}_\Gamma(\mathbf{X}, W)$ approximates the boundaries defined by Γ . The distance between the centre of the diametric ball and surface ball associated with a given edge e represents a Hausdorff metric $\epsilon_1(e)$, which tends to zero as the mesh density, and hence accuracy of approximation, are increased [31].

Here, we seek to give a concise definition of the restricted edges and surface triangles utilised in our meshing workflow. See table 4 for details.

5. GENERATING RESTRICTED TRIANGULATIONS

The first step in our meshing workflow is to form a restricted triangulation of the ellipsoidal mean-earth surface, conforming to the network of polyarc boundaries (coastlines, rivers, etc) inscribed on its surface. Our approach is an extension of the restricted Frontal-Delaunay scheme described in [10, 12], and related to previous restricted Delaunay refinement approaches due to, for example, Rineau and Yvinec [32], Cheng, Dey and Levine [30], Oudot, Rineau and Yvinec [33],

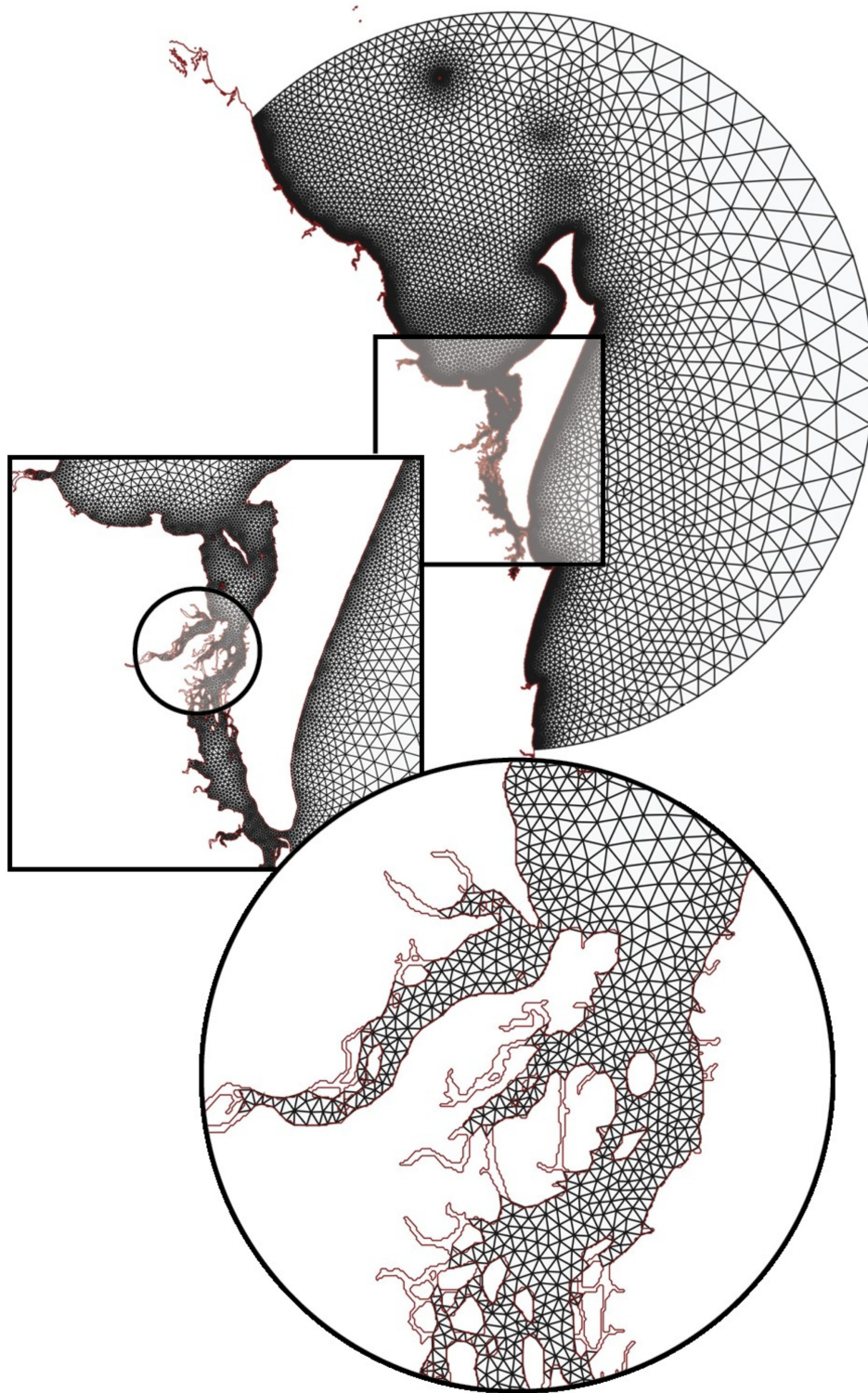


Figure 3: A restricted Laguerre triangulation of a coastal domain, showing a progressive zoom of the triangulation and the high-resolution polyline boundary to be meshed. Note the triangulation is not constrained to follow the high-resolution geometry exactly — it forms a ‘restricted’ approximation to it at the local length scales defined to resolve the physics of interest.

Table 4: Nomenclature for ‘restricted’ Laguerre-Power tessellations.

- \mathbf{X}, W : A set of weighted points in \mathbb{R}^3 , associated with the tessellation.
- $\text{Tri}(\mathbf{X}, W)$: The Laguerre triangulation of the points \mathbf{X}, W .
- $\text{Pow}(\mathbf{X}, W)$: The Power complex associated with the points \mathbf{X}, W .
- Γ, Σ : The input geometry: a collection of polyarc segments, and an ellipsoidal surface embedded in \mathbb{R}^3 .
- $\text{Tri}|_{\Gamma}(\mathbf{X}, W)$: The Laguerre sub-complex $\text{Tri}|_{\Gamma}(\mathbf{X}, W) \subseteq \text{Tri}(\mathbf{X}, W)$, restricted to Γ . $\text{Tri}|_{\Gamma}(\mathbf{X}, W)$ contains any edge $e \in \text{Tri}(\mathbf{X}, W)$ whose dual Power face $p_f \subseteq \text{Pow}(\mathbf{X}, W)$ intersects Γ .
- $\text{Tri}|_{\Sigma}(\mathbf{X}, W)$: The Laguerre sub-complex $\text{Tri}|_{\Sigma}(\mathbf{X}, W) \subseteq \text{Tri}(\mathbf{X}, W)$, restricted to Σ . $\text{Tri}|_{\Sigma}(\mathbf{X}, W)$ contains any cell $\tau \in \text{Tri}(\mathbf{X}, W)$ whose dual Power edge $p_e \subseteq \text{Pow}(\mathbf{X}, W)$ intersects Σ .
- $\rho_d(\tau)$: The radius-edge ratio associated with a d -simplex τ . Defined as the ratio of the radius of the circumball of τ to the length of its shortest edge.
- $\epsilon_1(e)$: The surface discretisation error associated with a 1-simplex $e \in \text{Tri}|_{\Gamma}(\mathbf{X}, W)$. Defined as the length from the centre of $\text{SDB}_1(e)$ to the centre of the diametric ball of e .
- $\text{SLB}_1(e)$: The surface Laguerre ball $B(\mathbf{c}_e, r)$ associated with an edge $e \in \text{Tri}|_{\Gamma}(\mathbf{X}, W)$. Balls are centred at intersections between the Power faces $p_f \in \text{Pow}(\mathbf{X}, W)$ and the arcs Γ , such that $\mathbf{c}_e = p_f \cap \Gamma$.
- $\bar{h}(\mathbf{x})$: The mesh-size function. A function $f(\mathbf{x}) : \mathbb{R}^3 \rightarrow \mathbb{R}^+$ defining the target edge length at points $\mathbf{x} \in \Sigma$.
- $a(f)$: The area-length ratio associated with a given triangle f . Defined as $a(f) = A/\|\mathbf{e}\|_{\text{rms}}^2$, where A is the signed area of f and $\|\mathbf{e}\|_{\text{rms}}$ is the root-mean-square edge length. The area-length ratio is a scalar measure of triangular element quality.

and Jamin, Alliez, Yvinec and Boissonnat [34].

5.1 Boundary discretisation

The refinement begins with a coarse sampling of the mean-earth spheroid — positioning 12 vertices over the surface to form a regular icosahedron. The restricted triangulation is then progressively refined, introducing new vertices to eliminate ‘poor-quality’ restricted edges in the mesh. An edge e is considered poor if:

- It is too long, such that $l_e \geq \alpha h(\mathbf{x}_e)$, where l_e is the length of the edge, $h(\mathbf{x}_e)$ is sampled at the edge midpoint and $\alpha = 4/3$ (by default).
- It does not approximate the domain geometry with sufficient accuracy, such that $\epsilon(e) \geq \beta h(\mathbf{x}_e)$, where $\epsilon(e)$ is the length of the perpendicular projection from the edge midpoint to the boundary Γ (the Hausdorff distance), $h(\mathbf{x}_e)$ is sampled at the edge midpoint and $\beta = 1/5$ (by default).
- (optional) It does not recover the correct topology of the true domain geometry.

If an edge is marked for refinement, a new vertex is inserted in the neighbourhood of its surface ball, the various restricted triangulations $\text{Tri}(\mathbf{X}, W)$ and $\text{Tri}|_{\Gamma}(\mathbf{X}, W)$ are updated incrementally, and the refinement continued. Here a ‘frontal’ refinement strategy is adopted, inserting a new ‘off-centre’ vertex along

Γ to satisfy local mesh spacing constraints, as per the approach described in [10]. This boundary refinement process is shown in the top panel of Figure 7.

To facilitate fast computation of intersections between the dual faces $p_f \in \text{Pow}(\mathbf{X}, W)$ and the arc segments Γ , the input geometry is stored in an AABB-tree. We assume the arcs in Γ describe ‘great ellipses’ — curves inscribed on a plane passing through the centre of the spheroidal earth. Such an assumption introduces a small error with respect to true geodesic curves defined on an ellipsoid, though the magnitude of this error given the eccentricity of the earth is vanishingly small.

5.2 Surface triangulation

Following the boundary discretisation pass, the interior of the domain is triangulated following a similar incremental frontal refinement approach. New vertices are introduced to eliminate ‘poor-quality’ restricted triangles in the mesh. A triangle τ is considered poor if:

- It is too large, such that $\sqrt{3}r_{\tau} \geq \alpha h(\mathbf{x}_{\tau})$, where r_{τ} is the radius of the circumscribing ball associated with τ , $h(\mathbf{x}_{\tau})$ is sampled at the centre of the ball, and $\alpha = 4/3$ (by default).
- It is of poor shape, such that $r_{\tau}/e_{\min} \geq \rho_{\tau}$, where r_{τ} is the radius of the circumscribing ball associated with τ , e_{\min} is the length of the shortest edge in τ , and the radius-edge threshold $\rho_{\tau} = 1.05$

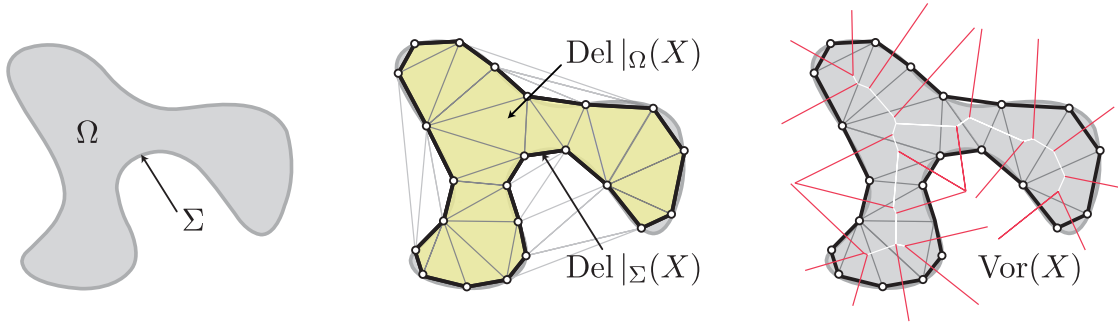


Figure 5: Restricted tessellations for a general domain $\Sigma \subset \mathbb{R}^2$, showing (a) the bounding curve $\Gamma \subset \Sigma$ and enclosed area Ω , (b) the ‘restricted’ meshes $\text{Tri}|_{\Gamma}(\mathbf{X}, W)$ and $\text{Tri}|_{\Sigma}(\mathbf{X}, W)$ that approximate the boundary Γ and domain interior Ω , and (c) the ambient Power diagram $\text{Pow}(\mathbf{X}, W)$. Dual Power edges that intersect with the boundary Γ are drawn in red. Here, $\text{Tri}|_{\Gamma}(\mathbf{X}, W)$ is a collection of edges and $\text{Tri}|_{\Sigma}(\mathbf{X}, W)$ a collection of triangles.

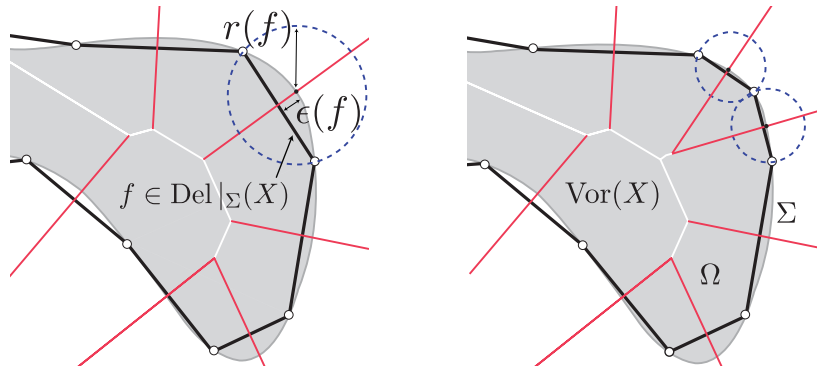


Figure 6: A restricted edge $e \in \text{Tri}|_{\Gamma}(\mathbf{X}, W)$ associated with a boundary arc Γ . In (a) it can be seen that edge e is restricted as its dual Power face $p_f \in \text{Pow}(\mathbf{X}, W)$ intersects the geometry Γ . The surface ball $B(\mathbf{c}_e, r)$ is centred at the point of intersection with Γ . In (b) the result of subdividing the boundary edge e is shown, with the new restricted edges and associated surface balls illustrated. Note the discretisation error $\epsilon_1(e)$ is decreased following the subdivision.

(by default). This constraint places an implicit bound on the angles in the mesh.

As per edge refinement, new vertices are inserted into the neighbourhood of circumscribing balls associated with poor quality triangles, and the restricted triangulations $\text{Tri}(\mathbf{X}, W)$ and $\text{Tri}|_{\Gamma}(\mathbf{X}, W)$ updated to reflect vertex updates. New vertices are positioned according to the ‘off-centre’ refinement rules described in [10], solving a local optimisation problem with respect to $h(\mathbf{x})$ and ρ_{τ} to position vertices ‘optimally’.

At completion, the resulting triangulation is a conforming mesh of the spheroidal domain, with the edges $\text{Tri}|_{\Gamma}(\mathbf{X}, W)$ approximating the imposed polycarc boundaries defined in Γ with a maximum Hausdorff error $\leq \beta h(\mathbf{x})$. The length of edges and size of triangles satisfies the mesh-spacing constraints $h(\mathbf{x})$, and the magnitude of triangle radius-edge ratios is

bounded below ρ_{τ} .

5.3 Discussion

The progress of the restricted triangulation algorithm described previously is demonstrated in Figure 7 for a simplified Earth system geometry in which global coastline constraints are specified. To illustrate the multi-scale nature of the restricted approach, the coastal geometry is defined in terms of $O(10\text{km})$ polycarcs, with the full mesh reconstructed at (uniform) $O(100\text{km})$ resolution.

The two panels in Figure 7 show the overall progress of the algorithm, as per the steps defined above. In Figure 7a, output from the boundary discretisation pass is shown, with vertices inserted along coastlines to re-sample the geometry at the coarse $O(100\text{km})$ mesh-spacing requested. The interior of the domain

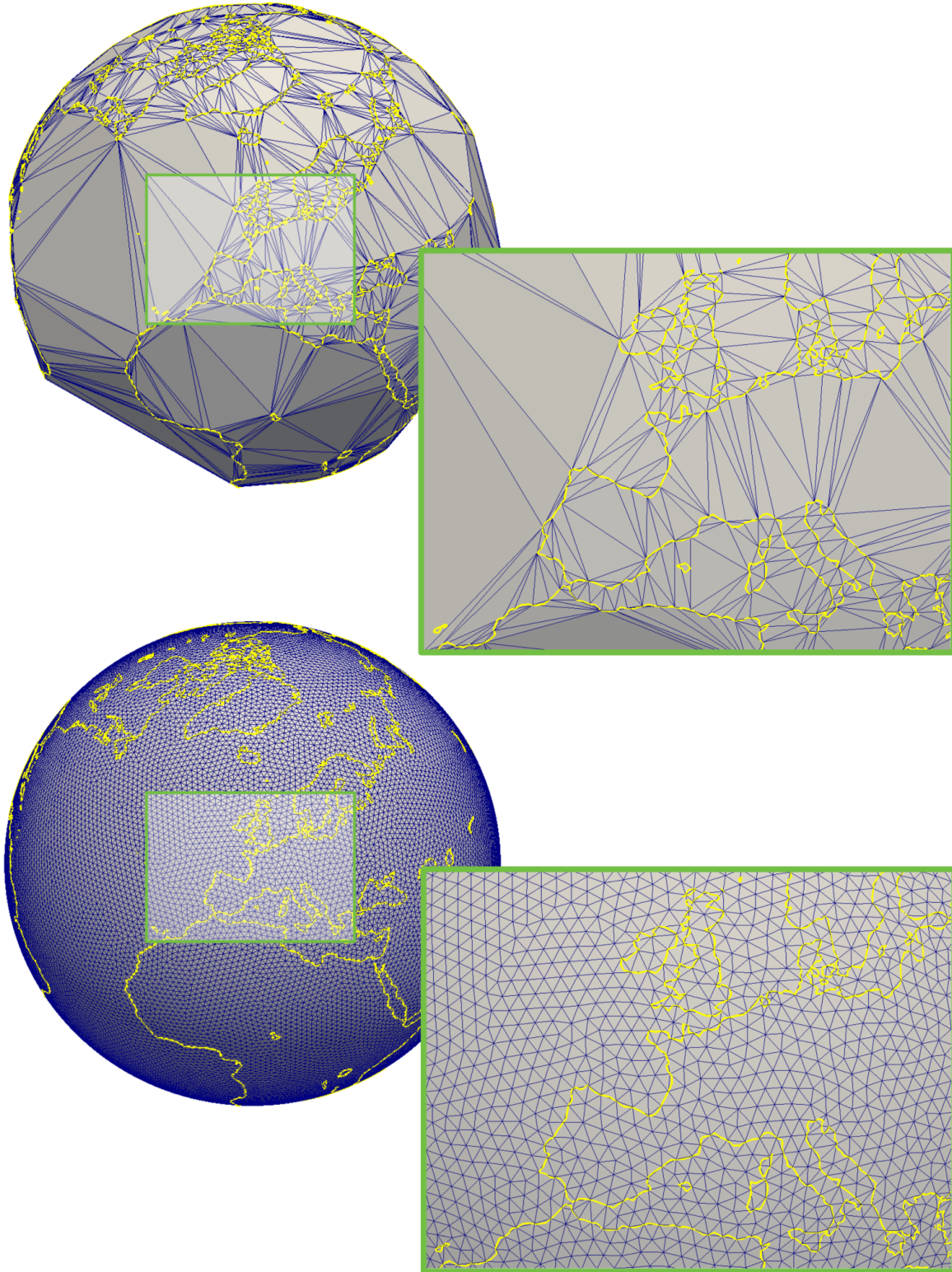


Figure 7: Snapshots of the restricted refinement process for an example spherical domain with coastlines and uniform mesh spacing constraints, showing the incremental discretisation of boundaries, followed by the triangulation of the interior. Close inspection of the inset panels shows the input geometry (yellow) is of higher resolution than the restricted triangulation (blue), demonstrating the resampling capabilities of the restricted meshing technique described.

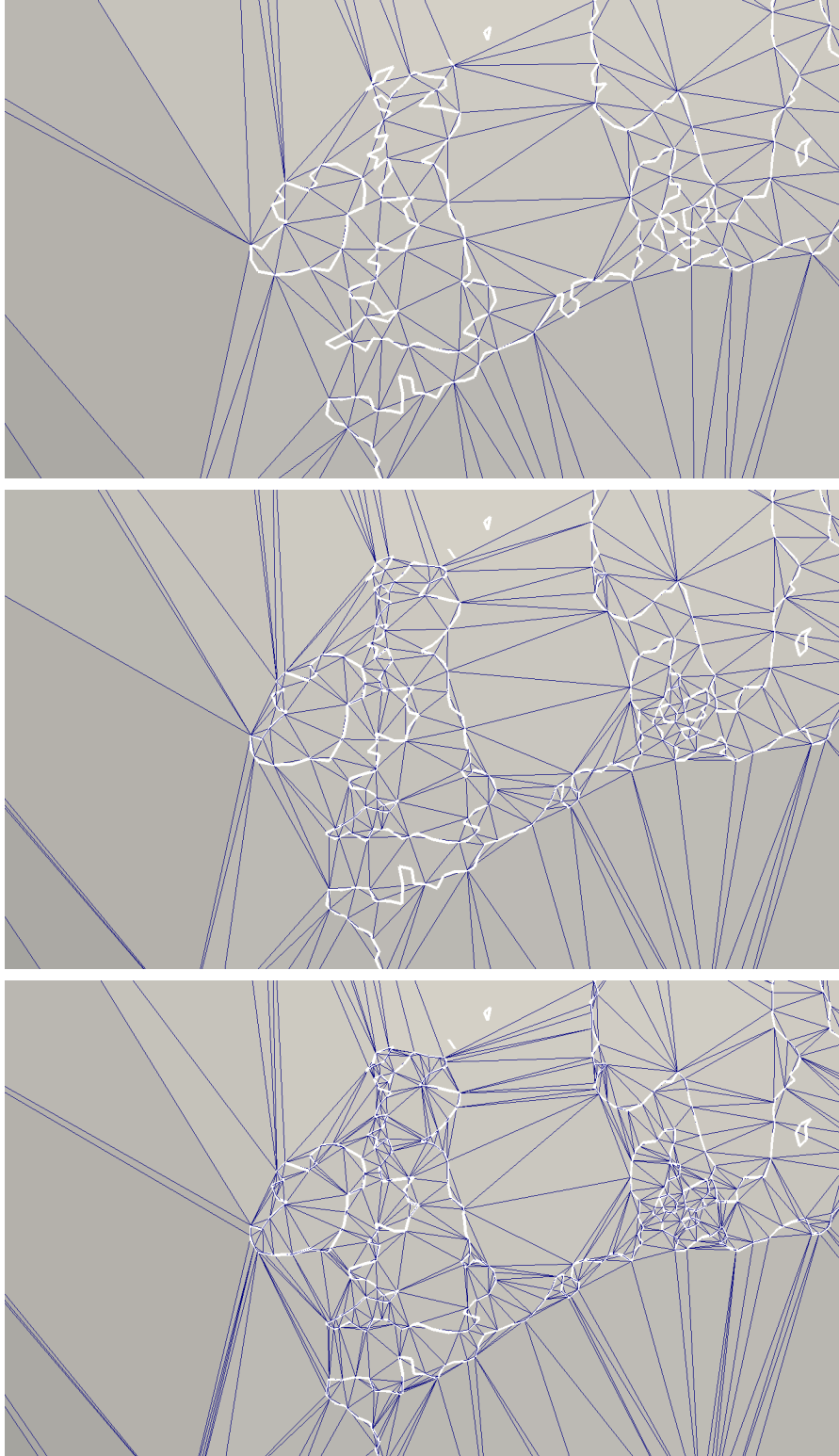


Figure 8: Sensitivity to the user-defined Hausdorff error metric ϵ_1 , showing the restricted tessellations of a subset of the coastal boundaries from Figure 7 with $\epsilon_1 = 1/3$ (upper), $\epsilon_1 = 1/10$ (middle) and $\epsilon_1 = 1/30$ (lower).

is a coarse tessellation of surface triangles spanning between coastal vertices. In Figure 7b, output from the subsequent surface triangulation pass is shown, consisting of a high-quality triangulation of the domain interior, conforming to the coarse boundary filtration constructed in the first phase. Note that despite imposing both mesh-spacing ($\bar{h}(\mathbf{x}) = 100\text{km}$) and triangle quality ($\bar{\rho} \leq 1.2$) constraints, no spurious over-refinement adjacent to the coastal boundaries is detected, confirming that the restricted triangulation approach can successfully be used to build high-quality, coarse-scale meshes that approximate complex geometrical domains on the sphere. Critically, these results show that use of restricted reconstructions can be used to efficiently ‘filter-out’ undesirable small and/or sharp features in specified geometry — leading to sparse meshes absent of small cells appropriate for computational simulation.

In Figure 8, sensitivity to the boundary discretisation error threshold ϵ_1 is analysed, with output from the initial boundary discretisation pass shown in three panels corresponding to $\epsilon_1 = 1/3, 1/10, 1/30$ from upper to lower. Recalling the discussion presented in Section 4, the boundary discretisation error ϵ_1 is a measure of the geometrical accuracy of the restricted filtration, based on a one-sided approximation to the Hausdorff distance between the restricted approximation to the boundary $\text{Tri}|_{\Gamma}(\mathbf{X}, W)$ and the true boundary Γ . As per Figure 8a, b, c, decreasing the threshold ϵ_1 leads to the expected increase in density, and hence accuracy, of the boundary sampling. Boissonnat and Oudot [31] have shown that the accuracy of the restricted approximation $\text{Tri}|_{\Gamma}(\mathbf{X}, W)$ approaches the true boundary Γ as the sampling density increases, therefore suggesting ϵ_1 as a simple, user-defined ‘tuning-knob’ that can be used to control the accuracy of the boundary reconstruction.

6. OPTIMISING LAGUERRE-POWER MESHES

After refinement, an optimisation phase is undertaken to further improve mesh quality — adjusting the position of vertices, the magnitude of vertex weights and the topology of the mesh to enhance the quality of the primal and dual cells with respect to the behaviour of the MPAS-type discretisation scheme described in Section 2 (viz. centroidal and well-centred configurations).

Given a Laguerre-Power tessellation $\text{Tri}(\mathbf{X}, W)$, a coupled optimisation problem is considered: adjust the points \mathbf{X} to maximise a variational mesh energy functional [22, 23, 24] to improve mesh shape and centroidalness, and the vertex weights W to maximise a primal-dual ‘cell staggering’ cost-function $Q^P(\mathbf{X}, W)$. The following is a generalisation of the planar meshing

workflow presented in [13] to surface tessellations on the ellipsoid.

6.1 Primal-dual cost function

Following [13], a primal-dual cost function can be defined to measure the geometrical ‘defect’ in the staggering between neighbouring cells and triangles. For each triangle τ_i

$$Q_i^P(\mathbf{X}, W) = \underbrace{\beta_f \left(1 - \left(\frac{\delta_f}{\bar{l}_f} \right)^2 \right)}_{\text{‘defect’ at face}} + \underbrace{\beta_e \left(\frac{1}{3} \sum_{e=1}^3 1 - \left(\frac{\delta_e}{l_e} \right)^2 \right)}_{\text{mean ‘defect’ at edges}}, \quad (1)$$

$$\delta_f = \|\mathbf{o}_f - \mathbf{m}_f\|, \quad \delta_{1,2,3} = \|\mathbf{o}_{1,2,3} - \mathbf{m}_{1,2,3}\|. \quad (2)$$

where the defect terms δ_f and δ_i measure the distance between the weighted triangle and edge circumcentres and the triangle and edge centroids \mathbf{m}_f and \mathbf{m}_i . These terms represent the geometrical ‘error’ associated with the staggering — a perfectly regular and centroidal primal-dual tessellation has $\delta_f = 0$ and $\delta_i = 0$. The lengths l_f and l_i are characteristic lengths associated with triangles and edges, with the l_i taken to be simple edge lengths and $\bar{l}_f = \frac{1}{3} \sum l_i$. We set the linear weights to be $\beta_f = 2/3$ and $\beta_e = 1/3$.

The function $Q_i^P(\mathbf{X}, W)$ aims to provide a combined measure of the quality of the staggering between primal and dual grid cells, with the first δ_f term in (1) accounting for the defect between the dual grid vertices and triangle centroids, and the second δ_e term the mean defect between dual grid edges and triangle edge midpoints. Maximisation of $Q_i^P(\mathbf{X}, W)$ is designed to improve the staggering between both primal-dual vertices and edge intersections in an average sense, leading to staggered mimetic discretisations of $\text{div}(\cdot)$, $\text{grad}(\cdot)$, and $\text{curl}(\cdot)$ with reduced discretisation error, as per [13].

6.2 Weight optimisation

Given a weighted mesh $\text{Tri}(\mathbf{X}, W)$, the weights can be optimised to maximise a primal-dual cost function

$$\text{find } W \subset \mathbb{R}, \text{ such that} \quad (3)$$

$$\min Q_i^D(\mathbf{X}, W) \quad \forall \tau_i \in \mathcal{T}(\mathbf{X}, W) \text{ is maximised.}$$

In general, (3) is a global, non-convex optimisation problem, with the weight at each vertex contributing to the cost $Q_k^P(\mathbf{X}, W)$, computed for all adjacent triangles $\tau_k \in \text{Tri}(\mathbf{X}, W)$. Rather than seeking direct solutions, a simple, locally-optimal approach is pursued here, influenced by the constrained, gradient-ascent type methods introduced for simplicial mesh

Algorithm 1 Weighted Optimisation Strategy

```

1: function OPTIMISEPRIMALDUAL( $\mathbf{X}, W, \mathcal{T}, \mathcal{D}$ )
2:   // Optimise a given primal-dual pair ( $\mathcal{T}, \mathcal{D}$ ), employing
3:   // a combination of geometrical, topological and weight-
4:   // based operations.
5:   for  $n = 1$  to  $N$  do // coupled outer iterations
6:     for  $m = 1$  to  $M$  do // vertex + weight updates
7:       for all  $x_i \in \mathcal{T}(\mathbf{X}, W)$  do // vertex updates
8:         Find update direction  $\mathbf{v}_i = \text{GRAD}_X((\mathbf{X}, W)^{m+1})$ 
9:         Perform line search  $\mathbf{x}_i^* \leftarrow \mathbf{x}_i^m + \Delta_i \mathbf{v}_i$ 
10:        Update  $\mathbf{x}_i^{m+1} \leftarrow \mathbf{x}_i^*$ , iff BETTER( $(\mathbf{X}, W)^*$ )
11:      end for
12:      for all  $w_i \in \mathcal{T}(\mathbf{X}, W)$  do // weight updates
13:        Find update direction  $v_i = \text{GRAD}_W((\mathbf{X}, W)^{m+1})$ 
14:        Perform line search  $w_i^* \leftarrow w_i^m + \Delta_i v_i$ 
15:        Update  $w_i^{m+1} \leftarrow w_i^*$ , iff BETTER( $(\mathbf{X}, W)^*$ )
16:      end for
17:    end for
18:    // Update grid topology
19:     $\mathcal{T}(\mathbf{X}, W)^{n+1} \leftarrow \text{FLIPTOPOLOGY}(\mathcal{T}(\mathbf{X}, W)^n)$ 
20:    // Refine/collapse edge
21:     $\mathcal{T}(\mathbf{X}, W)^{n+1} \leftarrow \text{PRUNEEDGES}(\mathcal{T}(\mathbf{X}, W)^{n+1})$ 
22:     $\mathcal{T}(\mathbf{X}, W)^{n+1} \leftarrow \text{REFINEEDGES}(\mathcal{T}(\mathbf{X}, W)^{n+1})$ 
23:  end for
24:  return optimised primal-dual complexes  $\mathcal{T}(\mathbf{X}, W)$  and  $\mathcal{D}(\mathbf{X}, W)$ 
25: end function

```

smoothing due to Freitag and Ollivier-Gooch [26] and Klinger and Shewchuk [27].

A steepest-ascent type update is employed for each vertex weight

$$w_i^{n+1} = w_i^n + \Delta_i^m v_i^n, \quad (4)$$

where

$$v_i^n = \frac{d}{dw_i} \mathcal{Q}_j^P(\mathbf{X}, W), \quad (5)$$

$$j = \text{argmin}_k \mathcal{Q}_k^P(\mathbf{X}, W) \forall \text{adj. } \tau_k \in \text{Tri}(\mathbf{X}, W).$$

Here, the index k is taken as a loop over the primal triangles $\tau_k \in \text{Tri}(\mathbf{X}, W)$ incident to \mathbf{x}_i . The scalar step length $\Delta_i^m \in \mathbb{R}^+$ is computed via a line search along the gradient ascent vector v_i and is taken as the first value that leads to an improvement in the worst-case quality metric $\mathcal{Q}_j^P(\mathbf{X}, W)$.

A simple bisection strategy is used to find the local step-length such that $\Delta_i^m = (\frac{1}{2})^m \Delta \bar{w}$, where m is the local line search iterate. The initial guess $\Delta \bar{w}$ is computed by considering a first-order Taylor expansion in local grid quality metrics

$$\mathcal{Q}_j^P(\mathbf{X}, W) + \Delta \bar{w} \frac{d}{dw_i} \mathcal{Q}_j^P(\mathbf{X}, W) \leq \bar{\mathcal{Q}}_k^P(\mathbf{X}, W). \quad (6)$$

Here, $\bar{\mathcal{Q}}_k^P(\mathbf{X}, W)$ is taken as a mean quality value over the local set of triangles $\tau_k \in \text{Tri}(\mathbf{X}, W)$, with the corresponding $\Delta \bar{w}$ an estimate of the weight perturbation required to improve the worst metric until it is equal to the local mean measure. A limited set of local iterations are employed, testing $m \leq 5$ until a successful step is found. If no such improvement is identified, the weight is left unchanged.

6.3 Variational scheme

Vertices in $\text{Tri}(\mathbf{X}, W)$, are updated using a variation on the Optimal Delaunay Triangulation (ODT) strategy due to Chen et al [24, 25]. In the standard ODT formulation, primal vertices are repositioned to minimise an element-wise *energy-functional*; leading to the optimal piecewise linear reconstruction of quadratic functionals. We modify the ODT procedure to incorporate the weighting of the Laguerre-Power structure replacing the triangle circumcentre terms in the ODT update with the weighted element orthocentres. This modification leads to a scheme in which primal vertex positions are updated as a weighted sum of the adjacent dual vertex coordinates — maintaining conceptual consistency with the conventional, un-

weighted ODT strategy. Adapting the ODT-style update strategy of Chen and Holst [25], primal vertices are repositioned such that

$$\mathbf{x}_i^{n+1} = (1 - \Delta_i^m) \mathbf{x}_i^n + \Delta_i^m \sum_{\tau_j \in *i} \frac{|\tau_j|_{\bar{h}}}{|*i|_{\bar{h}}} \mathbf{o}_j. \quad (7)$$

Here, $*i$ denotes the *star* of \mathbf{x}_i — the local set of elements $\tau_j \in \text{Tri}(\mathbf{X}, W)$ adjacent to \mathbf{x}_i . $|\tau_j|_{\bar{h}}$ denotes the *spacing-weighted* area of the triangle τ_j , and $|*i|_{\bar{h}}$ the summation of such terms over the set $*i$. The points \mathbf{o}_j are the weighted orthocentres associated with the triangles τ_j and Δ_i^m is a relaxation factor, computed via a local line search. In this study, the weighted-area factors are computed using a simple quadrature rule

$$|\tau_j|_{\bar{h}} = \int_{\tau_j} \frac{1}{\bar{h}(\mathbf{x})^2} dA \simeq \frac{A_j}{\bar{h}_j^2} \quad (8)$$

with $\bar{h}_j = \frac{1}{3} \sum_{\mathbf{x}_k \in \tau_j} \bar{h}(\mathbf{x}_k)$.

A local relaxation procedure is used to determine a quasi-optimal update. A series of local iterates are considered, setting $\Delta_i^m = (\frac{1}{2})^m$ for $m \leq 5$; terminating as soon the local element energy is improved.

6.4 Refinement & edge collapse

In addition to updates to the vertex positions and weights, in practice meshes may be further improved through the addition and/or removal of vertices. A set of *edge-refinement* and *edge-collapse* operations are introduced, applying the methodology presented in [13] to weighted primal-dual tessellations.

Given an edge e_k in the primal tessellation $\mathcal{T}(\mathbf{X}, W)$, a *collapse* operation is achieved by *merging* the two vertices $\{x_i, x_j\} \in e_k$ to a local mean position \mathbf{x}_m and re-triangulating the local cavity $\mathcal{C}_k \subseteq \mathcal{T}(\mathbf{X}, W)$ incident to the edge. In the present work, vertices are merged to an average of adjacent element orthocentre coordinates, such that $\mathbf{x}_m = \frac{1}{|\mathcal{C}_k|} \sum \mathbf{o}_i$ for all local triangles $\tau_i \in \mathcal{C}_k$.

Given an edge e_k in the primal tessellation $\mathcal{T}(\mathbf{X}, W)$, a *refinement* operation is achieved by inserting a new vertex x_n , positioned at the centre of the orthoball associated with the lower quality adjacent triangle $\tau_i \in \mathcal{T}(\mathbf{X}, W)$. Insertion of the new vertex x_n induces a re-triangulation of the local cavity $\mathcal{C}_k \in \mathcal{T}(\mathbf{X}, W)$; constructed by expanding about x_n in a local greedy fashion. Starting from the initial cavity $\mathcal{C}_k = \{\tau_i, \tau_j\}$, where $\{\tau_i, \tau_j\} \in \mathcal{T}(\mathbf{X}, W)$ are the triangles adjacent to the edge e_k , additional elements are added to the cavity \mathcal{C}_k in a breadth-first manner, with a new, unvisited neighbour τ_k added if doing so will improve the worst-case grid-quality metric $\mathcal{Q}^T(\mathbf{X})$ of the re-triangulated configuration.

6.5 Weighted optimisation schedule

The full primal-dual grid optimisation procedure is realised as a combination of various geometrical and topological operations; organised into a particular iterative sequence. See Algorithm 1 for details. Each outer iteration consists of a fixed set of operations: eight sweeps to update vertex positions and weights, an iterative edge-flipping scan to restore the local Laguerre weighted in-sphere criterion, and, finally, a single pass of edge refinement/collapse operations. In this study, a maximum of sixteen outer iterations were employed. Each vertex- and weight-update pass is implemented as a composite operation, with the variational ODT-style technique supplemented with the local gradient-ascent iterations as required. Given a vertex \mathbf{x}_i in the primal mesh, an ODT-like update is always attempted first, with a subsequent gradient-ascent step employed only in cases where local grid-quality metrics are not sufficiently improved by the initial step. Updates to the vertices \mathbf{X} and weights W occur sequentially, with a single, linear sweep over the grid vertices followed by a single pass over the mesh weights. Each vertex- and weight-update pass is arranged to follow a symmetric Gauss-Seidel philosophy, with vertices and weights visited symmetrically in a pair of forward and reverse passes. The optimisation schedule employed here is not based on a particular theoretical derivation, but is simply a heuristic that has proven to be effective in practice, building on well-known hybrid optimisation approaches [26, 27].

7. INITIAL RESULTS

The performance of the Laguerre-Power algorithm presented here has been investigated experimentally, with the method used to generate a ‘unified’ ocean-river-land mesh, focused on the US Mid-Atlantic coast region. Such configurations will be used in upcoming simulations at the US Department of Energy to study coupled climate response in the Delaware and Chesapeake Bay areas, and the US North-East coast. Our algorithms are implemented as part of the **JIGSAW** package, currently available online [11] or by request from the author. The algorithm was implemented in C++ and compiled as a single-threaded 64-bit executable.

Initial results are shown in Figure 9, illustrating both the global mesh for the full earth domain, as well as local detail adjacent to the coast in the area of study. In addition to a mesh of the ocean and land surface domains, cells align with the embedded coastline and river boundaries in a conforming sense, facilitating coupling between the various ocean, river and land physics components within the E3SM framework.

The use of the restricted triangulation kernel was critical for this domain — the coastline and river bound-

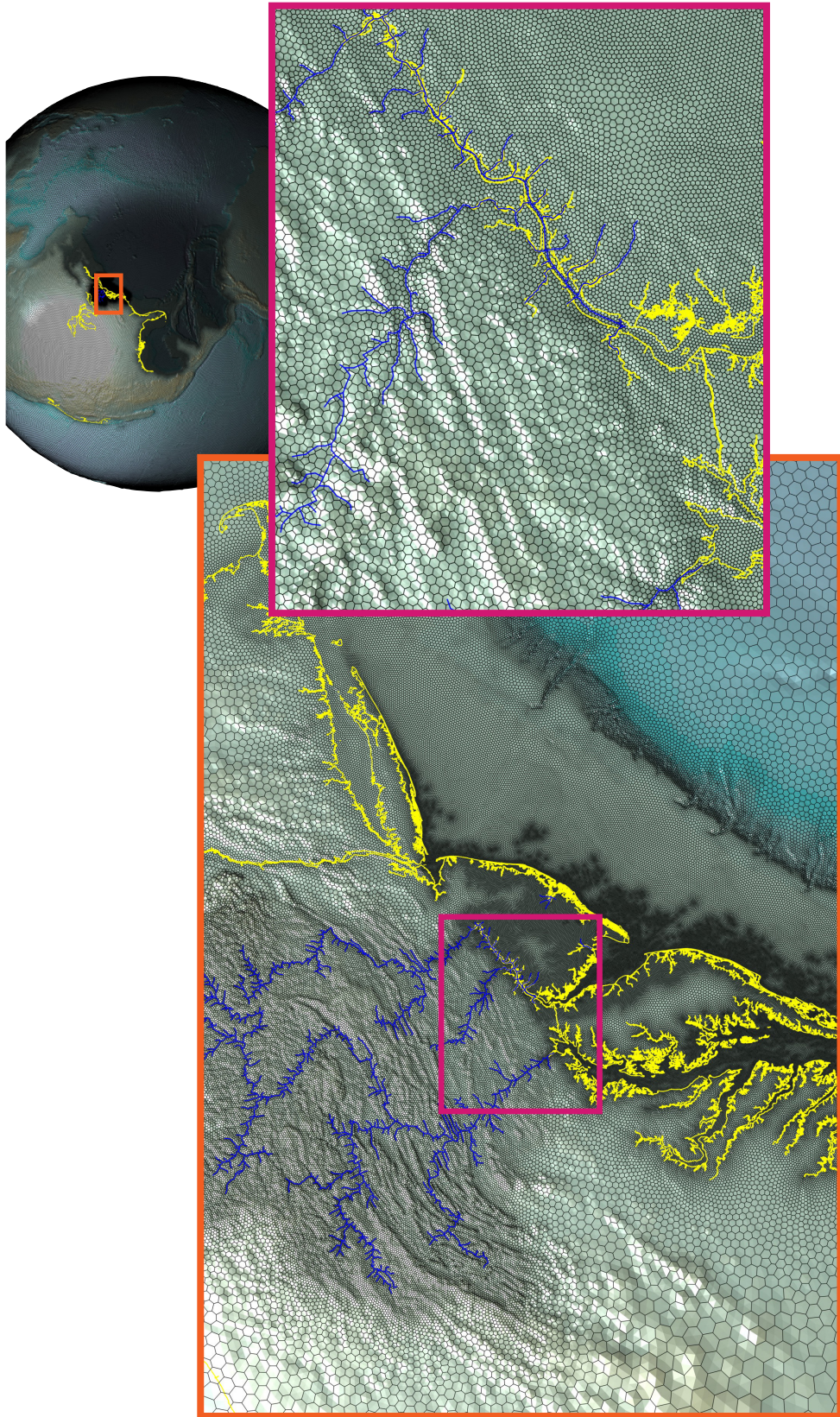


Figure 9: A restricted Laguerre triangulation of a coastal ocean-river-land domain on the sphere, showing progressive zoom into the Delaware and Chesapeake Bay areas on the US Mid-Atlantic coast. Note that cells align with imposed coastline and river-network boundaries, with rivers routed across cell faces, consistent with the normal flow direction.

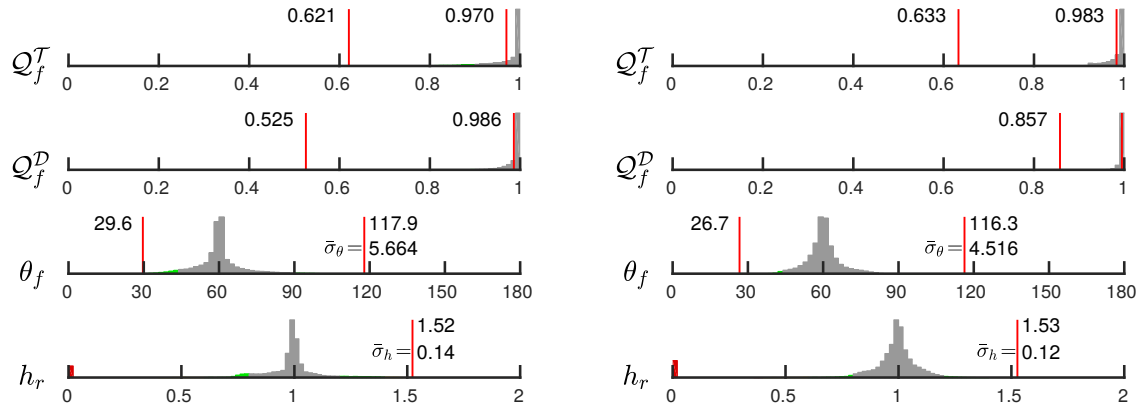


Figure 10: Histograms of mesh quality metrics for Figure 9, before and after the application of the weighted Laguerre-Power mesh optimisation scheme. Q_f^T is the triangle area-length ratio, Q_f^D is the primal-dual metric defined in Section 6, θ_f is the distribution of angles in the triangle cells, and h_r is a measure of relative conformance to the imposed mesh-spacing function $h(\mathbf{x})$. Histograms are taken over all cells in the mesh.

aries were specified via very high-resolution ($\approx 30\text{m}$) geoscientific data-sets, containing various small, sharp, and otherwise undesirable features. The domain was re-meshed according to a non-uniform mesh-spacing pattern $h(\mathbf{x})$, designed to capture both regional and local scale physics in the ocean, land, and river catchment regions, with additional refinement used to resolve sharp changes in the land and ocean bottom surface elevation (see for example [4] for additional detail). The minimum mesh-length is $O(1\text{km})$, demonstrating the capabilities of the restricted triangulation approach to ‘up-scale’ high-resolution geometry inputs and obtain simplified, high-quality meshes at length scales of interest to the user.

Application of the weighted mesh optimisation scheme led to significant improvements in mesh-quality, improving both the shape and centroidal characteristics of the triangulation in a conventional sense, as well as the quality of the primal-dual staggering, with the accuracy of the mimetic MPAS-type discretisation in mind. See Figure 10 for detail. The unoptimised mesh generated by the restricted triangulation kernel contained approximately 10,000 cells (out of 800,000 total) that were not well-centred, with the vertices of polygonal cells lying outside the hull of their associated dual triangles. The development of strategies to deal with such ‘trapped’ cells is an avenue for future work.

Use of the weighted optimisation scheme reduced the number of not-well-centred to just two, with both of these triangles consisting of configurations in which all vertices were located on boundary constraints, making further optimisation difficult. As per Figure 10, the weighted mesh optimisation scheme led to improvements in various primal and dual quality metrics, lead-

ing to a mesh with enhanced centroidal characteristics and distribution of cell angles. The overall computational burden of the coupled optimisation scheme is, in our view, not constraining — for the 800,000 cell mesh shown, total (single-core) run-time is approximately 20 minutes, with the initial refinement of the restricted triangulation taking around 90 seconds, and the mesh optimisation the remaining time. Within the optimisation kernel itself, approximately 50% of time is spent updating vertex positions, 25% vertex weights, and the remaining 25% spread across the various edge-collapse/refinement and topology updates.

ACKNOWLEDGEMENTS

This work was supported by the Earth System Model Development and Regional and Global Modeling and Analysis program areas of the U.S. Department of Energy, Office of Science, Office of Biological and Environmental Research as part of the multi-program, collaborative Integrated Coastal Modeling (ICoM) project.

CODE AVAILABILITY

The JIGSAW mesh generation package used in this study is available online: <https://github.com/dengwirda/jigsaw>. In addition to the underlying C++ library, bindings for both MATLAB: <https://github.com/dengwirda/jigsaw-matlab> and Python: <https://github.com/dengwirda/jigsaw-python> are available.

References

- [1] Caldwell, Peter M., et al., The DOE E3SM coupled model version 1: Description and results at high resolution. *Journal of Advances in Modeling Earth Systems* 11.12 (2019): 4095-4146.
- [2] T. Semmler, S. Danilov, P. Gierz, H. Goessling, J. Hegewald, C. Hinrichs, N. Koldunov, N. Khosravi, L. Mu, T. Rackow, D. Sein, D. Sidorenko, Q. Wang, T. Jung, Simulations for CMIP6 with the AWI Climate Model AWI-CM-1-1, *Journal of Advances in Modeling Earth Systems*, 12 (9) (2020), 1942–2466.
- [3] J. Thuburn, C. Cotter, and T. Dubos, A mimetic, semi-implicit, forward-in-time, finite volume shallow water model: comparison of hexagonalicosahedral and cubed-sphere grids, *Geosci. Model Dev.*, 7 (2014) 909–929.
- [4] W. Pringle, D. Wirasaet, K. Roberts, and J. Westerink, Global storm tide modeling with ADCIRC v55: unstructured mesh design and performance, *Geosci. Model Dev.*, 14 (2021) 1125–1145.
- [5] P. Memari, P. Mullen, M. Desbrun, Parametrization of generalized primal-dual triangulations, in: *Proceedings of the 20th International Meshing Roundtable*, Springer, 2011, pp. 237–253.
- [6] P. Mullen, P. Memari, F. de Goes, M. Desbrun, HOT: Hodge-optimized triangulations, *ACM Transactions on Graphics (TOG)* 30 (4) (2011) 103.
- [7] F. d. Goes, P. Memari, P. Mullen, M. Desbrun, Weighted triangulations for geometry processing, *ACM Transactions on Graphics (TOG)* 33 (3) (2014) 28.
- [8] S. Walton, O. Hassan, K. Morgan, Advances in co-volume mesh generation and mesh optimisation techniques, *Computers & Structures* 181 (2017) 70–88.
- [9] J. R. Shewchuk, Triangle: Engineering a 2D quality mesh generator and Delaunay triangulator, in: *Applied computational geometry towards geometric engineering*, Springer, 1996, 203–222.
- [10] D. Engwirda, D. Ivers, Off-centre Steiner points for Delaunay-refinement on curved surfaces, *Computer-Aided Design* 72 (2016) 157–171.
- [11] D. Engwirda, JIGSAW: An unstructured mesh generation package, <http://www.github.com/dengwirda/jigsaw> (2016).
- [12] D. Engwirda, JIGSAW-GEO (1.0): locally orthogonal staggered unstructured grid generation for general circulation modelling on the sphere, *Geoscientific Model Development* 10 (6) (2017) 2117.
- [13] D. Engwirda, Generalised primal-dual grids for unstructured co-volume schemes. *Journal of Computational Physics* 375 (2018): 155-176.
- [14] F. Aurenhammer, Power diagrams: properties, algorithms and applications, *SIAM Journal on Computing* 16 (1) (1987) 78–96.
- [15] H. Edelsbrunner, *Algorithms in combinatorial geometry*, Vol. 10, Springer Science & Business Media, 2012.
- [16] T. Ringler, J. Thuburn, J. Klemp, W. Skamarock, A unified approach to energy conservation and potential vorticity dynamics for arbitrarily-structured C-grids, *Journal of Computational Physics* 229 (9) (2010) 3065–3090.
- [17] T. Ringler, M. Petersen, R. Higdon, D. Jacobsen, P. Jones, M. Maltrud, A multi-resolution approach to global ocean modeling, *Ocean Modelling* 69 (2013) 211–232.
- [18] J. Thuburn, T. Ringler, W. Skamarock, J. Klemp, Numerical representation of geostrophic modes on arbitrarily structured C-grids, *Journal of Computational Physics* 228 (22) (2009) 8321 – 8335.
- [19] W. C. Skamarock, J. B. Klemp, M. G. Duda, L. D. Fowler, S.-H. Park, T. D. Ringler, A multiscale nonhydrostatic atmospheric model using centroidal Voronoi tessellations and C-grid staggering, *Monthly Weather Review* 140 (9) (2012) 3090–3105.
- [20] E. Vanderzee, A. N. Hirani, D. Guoy, E. Ramos, Well-centered planar triangulation—an iterative approach, in: *Proceedings of the 16th International Meshing Roundtable*, Springer, 2008, pp. 121–138.
- [21] E. Vanderzee, A. N. Hirani, D. Guoy, E. A. Ramos, Well-centered triangulation, *SIAM Journal on Scientific Computing* 31 (6) (2010) 4497–4523.
- [22] Q. Du, V. Faber, M. Gunzburger, Centroidal Voronoi tessellations: applications and algorithms, *SIAM review* 41 (4) (1999) 637–676.
- [23] P. Alliez, D. Cohen-Steiner, M. Yvinec, M. Desbrun, Variational tetrahedral meshing, in: *ACM Transactions on Graphics (TOG)*, Vol. 24, ACM, 2005, pp. 617–625.

- [24] L. Chen, J.-C. Xu, Optimal Delaunay triangulations, *Journal of Computational Mathematics* (2004) 299–308.
- [25] L. Chen, M. Holst, Efficient mesh optimization schemes based on optimal Delaunay triangulations, *Computer Methods in Applied Mechanics and Engineering* 200 (9) (2011) 967–984.
- [26] L. A. Freitag, C. Ollivier-Gooch, Tetrahedral mesh improvement using swapping and smoothing, *International Journal for Numerical Methods in Engineering* 40 (21) (1997) 3979–4002.
- [27] B. M. Klingner, J. R. Shewchuk, Aggressive tetrahedral mesh improvement, in: *Proceedings of the 16th international meshing roundtable*, Springer, 2008, pp. 3–23.
- [28] H. Edelsbrunner, N. R. Shah, Triangulating Topological Spaces, *International Journal of Computational Geometry & Applications* 7 (04) (1997) 365–378.
- [29] S. W. Cheng, T. K. Dey, J. R. Shewchuk, *Delaunay Mesh Generation*, Taylor & Francis, New York, 2013.
- [30] S. Cheng, T. Dey, Quality Meshing with Weighted Delaunay Refinement, *SIAM Journal on Computing* 33 (1) (2003) 69–93.
- [31] J. D. Boissonnat, S. Oudot, Provably Good Sampling and Meshing of Surfaces, *Graphical Models* 67 (5) (2005) 405–451.
- [32] L. Rineau, M. Yvinec, Meshing 3D Domains Bounded by Piecewise Smooth Surfaces, in: M. L. Brewer, D. Marcum (Eds.), *Proceedings of the 16th International Meshing Roundtable*, Springer Berlin Heidelberg, Berlin, Heidelberg, 2008, pp. 443–460.
- [33] S. Oudot, L. Rineau, M. Yvinec, Meshing Volumes Bounded by Smooth Surfaces, in: *Proceedings of the 14th International Meshing Roundtable*, Springer, 2005, pp. 203–219.
- [34] C. Jamin, P. Alliez, M. Yvinec, J.-D. Boissonnat, CGALmesh: a generic framework for delaunay mesh generation, *ACM Transactions on Mathematical Software (TOMS)* 41 (4) (2015) 23.